CONF-9008186--1

Invited paper for the

Proceedings of ICTP Working Party on *Electrochemistry*
Trieste, Italy
August 17–September 7, 1990

CONF-9008186--1

DE91 007181

THEORY OF BULK AND INTERFACE CONSTANT PHASE ELEMENTS IN ELECTRODE-ELECTROLYTE SYSTEMS

S. H. LIU

DISCLAIMER

SOLID STATE DIVISION
OAK RIDGE NATIONAL LABORATORY
Operated by
MARTIN MARIETTA ENERGY SYSTEMS, INC.
Under
Contract No. DE-AC05-84OR21400
With the
U.S. DEPARTMENT OF ENERGY
Oak Ridge, Tennessee 37831

January 1991

THEORY OF BULK AND INTERFACE CONSTANT PHASE ELEMENTS IN ELECTRODE-ELECTROLYTE SYSTEMS

S. H. LIU
Solid State Division, Oak Ridge National Laboratory
Oak Ridge, Tennessee 37831-6032, USA

ABSTRACT

This paper summarizes the progress gained in the last few years in our understanding of bulk and interface constant-phase-angle (CPA) behavior in electrode-electrolyte systems. It is now fairly well established that the interface constant-phase element originates from the fractal nature of the interface. The complex geometry gives rise to a fractal distribution of parallel current paths, and the competition between these paths results in the fractional power law behavior of the impedance across the interface. On the other hand, the early hope of relating the CPA exponent to the fractal dimension of the interface has been shown to be unattainable. Our understanding of the bulk CPA behavior, which is most prevalent in solid electrolytes, is only tentative. It is illustrated using a simple model that, under nonlinear dynamical laws that govern the flow of ions in the electrolyte, a current in the solid can generate a fractal distribution of vacancies which tend to impede the flow. The current is forced to negotiate a complex path through the solid, and the resulting fluctuation in path length and flow rate could be a source of the CPA behavior.

1. Introduction

Impedance spectroscopy is a simple and powerful tool for probing the physical and chemical properties of electrode-electrolyte systems. In a typical experiment an ac current is sent through the system and the voltage drop across the system is measured. From the frequency dependence of the impedance, one tries to infer the combination of known circuit elements–resistance, inductance and capacitance–which reproduces the measured behavior. The interpretation of these circuit elements gives insight into the various physical and chemical reactions taking place in the system.

Simple as the program may sound, it is difficult to carry out because the behavior of real systems cannot be modelled by a finite number of circuit elements, no matter how they are chosen. The difficulty lies in the constant-phase behavior, which necessitates the inclusion of a mysterious circuit element whose impedance has the power-law frequency dependence:

$$Z(\omega) \propto (j\omega)^{-\eta}, \tag{1}$$

where $j = \sqrt{-1}$, ω is the angular frequency, and the exponent η satisfies $0 < \eta < 1$. Fig. 1 shows a set of actual data taken at the Oak Ridge National Laboratory.[1,2]

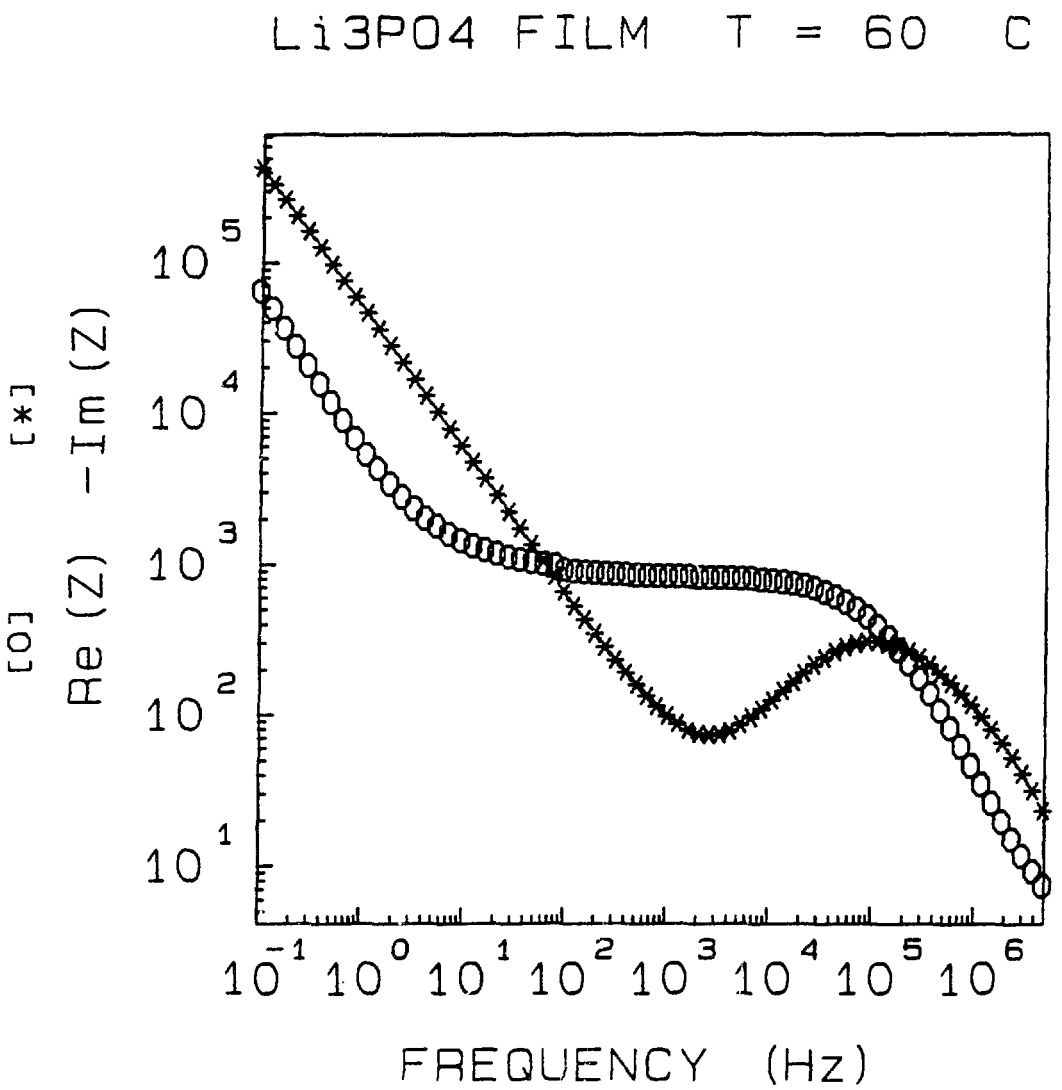

Fig. 1. The real and imaginary parts of the impedance of a 1 μm amorphous Li_3PO_4 film with gold electrodes plotted as functions of the frequency in log-log scale.

In this figure the real and imaginary parts of $Z(\omega)$ of a 1μm amorphous Li_3PO_4 film with gold electrodes are plotted against the frequency ($f = \omega/2\pi$) in log-log scale. Straight lines on the graph with negative slope indicate power-law frequency dependence. In particular, when real and imaginary parts form two parallel lines, it is an unmistakable indication of CPA behavior. One finds two regions in Fig. 1 in which CPA behavior is apparent: at the low frequency end below 3 Hz and at the high frequency end above 10^5 Hz. At the low frequency end where the CPA component of the impedance is overwhelming, one can extract the exponent η from the data in two ways: from the slope of the straightline portion of the data, or from the constant ratio

$$-ImZ(\omega)/ReZ(\omega) = \tan(\eta\pi/2). \tag{2}$$

The last property gives the name constant-phase-angle, i.e. the argument of tangent function in the above equation, to the mysterious circuit element, which is also called constant-phase element (CPE). At the high frequency end the CPA exponent must be determined from curve fitting because of the large background. To fit the data in Fig. 1 one needs two constant-phase elements, one with $\eta \simeq 0.92$ at the low frequency end and one with $\eta \simeq 0.77$ at the high frequency end.[2] Through carefully controlled experiments, it has been determined that the low frequency CPE originates from physical processes taking place at the interface while the high frequency one originates from interactions in the bulk of the electrolyte. In the complex ω plane the CPA impedance has a branch cut along the positive imaginary axis. This analytic property cannot be reproduced by any finite combination of RLC elements because the impedance of the combination can only have a finite number of poles, never a branch cut. The only known examples of branch cuts are infinite ladder networks and transmission lines, both having $\eta = 1/2$. Attempts have been made to concoct infinite ladder networks with varying RC elements or transmissions line with spatially varying RC distributions to simulate the interfacial CPE,[1-3] but one then faces the challenge of how to justify the concoction on physical grounds. For the bulk CPE one must assume a continuous distribution of activation energies for ion hopping.[4] Again, no explanation of the origin of the distribution has been offered.

In the last few years we have witnessed significant progress toward a qualitative to semi-quantitative understanding of the interfacial CPE. It is now fairly well established that the behavior has its origin in the fractal geometry of the inherently rough interface. The understanding of bulk CPE is comparatively rudimentary. It seems that a theory based on self-organized fractal geometry holds promise as a possible explanation. This paper contains a review of these recent developments, with emphasis not on data fitting but on elucidating the processes which lead to the CPA behavior.

2. Theory of Interfacial CPE

The ideal electrode-electrolyte interface as discussed in textbooks in electrochemistry consists of a planar metal electrode in contact with the electrolyte. Consider a blocking electrode where no chemical reaction takes place, a bias potential across the interface causes a surface charge to accumulate on the metal and a screening cloud of the opposite charge to form in the electrolyte. The combination of charge distributions creates an interfacial capacitance. A probing ac signal encounters an impedance which consists of the ohmic resistance in the electrolyte and the interfacial capacitance. The ohmic resistance in the metal electrode can be ignored. Therefore, the real part of the total impedance should be frequency independent and the imaginary part should be inversely proportional to the frequency. The observation that this simple theory does not apply to real interfaces was first made in 1926.[5] In recent years it has become increasingly clear that the interface, no matter how carefully it is prepared, is uneven on the submicron scale, and the CPA behavior is intimately linked to the microscopic roughness.[6–10] When the interface is made increasingly smooth, the value of η approaches unity.

A logical connection between roughness and fractional power-law impedance was first suggested by Le Méhauté who pointed out that rough surfaces are fractals, i.e. the roughness looks the same under different degrees of magnification.[11] Before we present his argument and the subsequent development of this idea by other authors, we make a brief digression to define what a fractal is in terms readily understandable by physical scientists. A good example of a fractal object is the monster curve known as the Koch island, which is constructed by the procedure illustrated in Fig. 2. One begins with an equilateral triangle. Next, one divides each side into three parts and erects an equilateral triangle using the middle part as the base. This results in the six-fold symmetric star. In the third stage the twelve sides of the star are trisected and smaller equilateral triangles are erected in the middle of each. The Koch island is constructed by repeating this procedure *ad infinitum*. The boundary of the island is obviously continuous, but is not differentiable because it makes an infinite number of zigzags between every two points on the curve. The length of the curve between any two points is infinity, but the area of the island is finite. A small part of the curve is similar to a larger part when magnified by any integral powers of 3. This property, called self-similarity under a scale transformation, is common to all fractal objects. Other examples of fractals can be found in the two books by Mandelbrot.[12,13] Fractals in nature are not as regular as the Koch island. They usually appear random, but are self-similar in a statistical sense, that is, given a sufficiently large sample of similar objects, the magnification of a small part of one object can be matched arbitrarily closely with some other object. The scale of magnification can be arbitrary. The range of length in which self similarity holds is bounded from above by the size of the object and from below by the size of the smallest building block, an atom for example.

The term "fractal dimension" describes the self-similar property under scale transformation in a quantitative manner. This concept, first proposed by Hausdorff

ORNL-DWG 84-16474

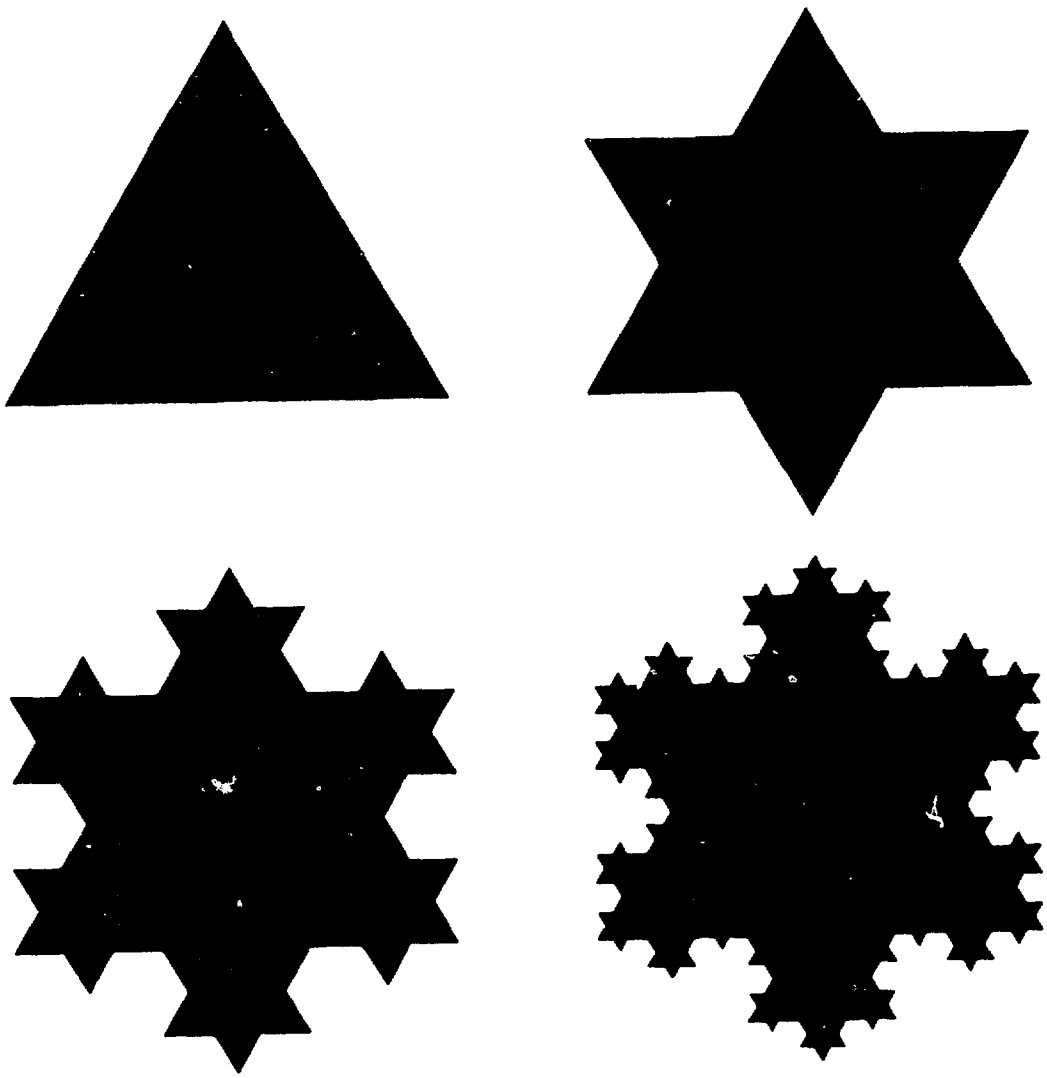

Fig. 2. The first four stages in the construction of the Koch island. In the fractal infinite stages, the boundary of the island is of fractal dimension $d = \ln 4/\ln 3 = 1.2619$.

in 1919, is a direction generalization of dimension in Euclidean geometry. When the sides of a square are magnified by a factor of 2, the area is 4 times larger. If we write $4 = 2^d$, we find that $d = 2$ is the dimension of the area. Similarly, the volume of a cube is 8 times larger under a similar magnification of its sides. This gives $d = \ln 8/\ln 2 = 3$ as the dimension of the volume. Going back to the Koch island in Fig. 2. The process of constructing the fourth stage from the third may be regarded in a slightly different way, that is, the two stages are images of the same object viewed with different degrees of magnification. In the third stage the resolution only allows us to see 48 straight segments forming the boundary but not the smaller features within each segment. In the next stage all lengths are magnified 3 times so that the same resolution allows us to resolve each segment into 4 because the middle third now appears to consist of two segments. Details beyond this level cannot be resolved. A similar definition, $4 = 3^d$ or $d = \ln 4/\ln 3 = 1.2619$ is the dimension of the Koch curve. We obtain the same result by holding the length scale constant but improving the resolution. The total length of the curve appears to be 4 times larger every time the resolution is improved threefold. In the limit of infinite resolution the length diverges, as discussed previously. The area of the Koch island remains two dimensional because it has a finite limiting value.

Fractals need not be monster curves. An example, the Cantor bar, is shown in Fig. 3. Under coarse resolution the object looks like a continuous bar. With improved resolution one sees a gap in the middle which separates the bar into two, each is $1/a$ the length of the original bar, $a > 2$. With higher resolution each one of the bars is seen to be subdivided in the same manner. The dimension of the object is $d = \ln 2/\ln a < 1$. Under infinite resolution the object seems to disappear because it has a dimension less than the dimension of the Euclidean space it is imbedded.

In Fig. 4 we show the electron micrograph of a surface of the solid electrolyte Ag β-alumina,[10] which is a good example of the electrode-electrolyte interface. There are hills and valleys of various sizes, and each hill has smaller hills and valleys of various sizes so that the picture looks the same under different magnifications. The fractal dimension of such a surface is larger than 2, which means that the observed area increases with increasing resolution. Many real surfaces have the property that self similarity is achieved by scaling the height in a ratio different from the lengths in the plane of the surface. This type of scale invariance is called self affinity. The surface depicted in Fig. 4 is actually self-affine, but the electron micrograph does not convey adequately the depth information of the surface features. Notice that although every fractal object has a well-defined dimension in a range of length scales, the fractal dimension does not contain sufficient information about the fractal. Fractals with the same dimension may look distinctly different.

The first model for rough interface was the surface traced out by shifting the Koch island in the direction perpendicular to the plane of the shape.[11] An area on the surface is bounded by Koch curves in one direction and straight lines in the perpendicular direction. Since the area is measured by the product of the lengths of the boundary curves in the two directions, the dimension of the surface is the sum of the dimensions of the boundary curves, $d = 1 + \ln 4/\ln 3 = 2.2619$. Le Méhauté

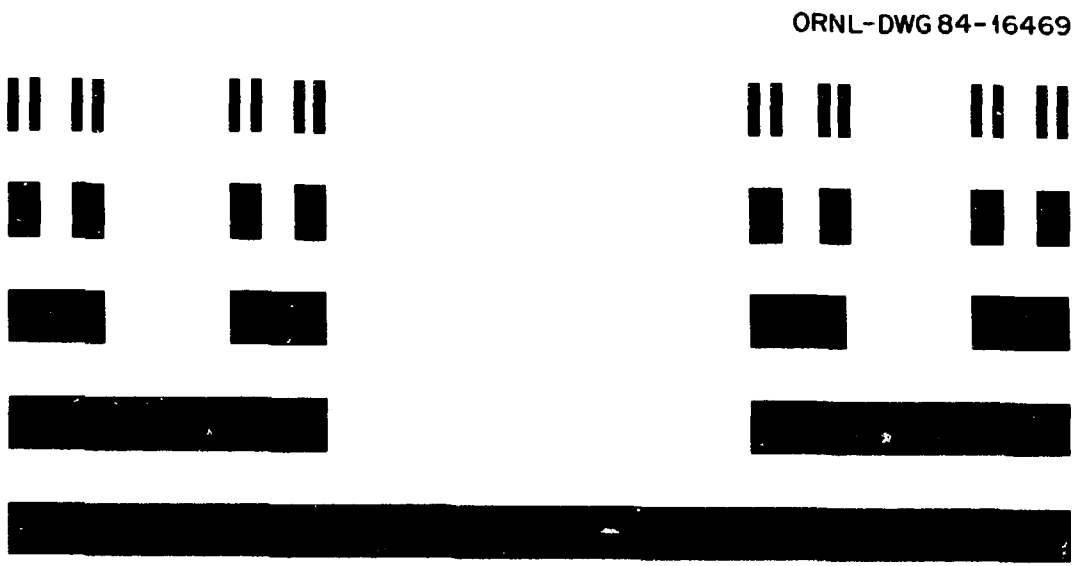

Fig. 3. The first fives stages in the construction of a Cantor bar.

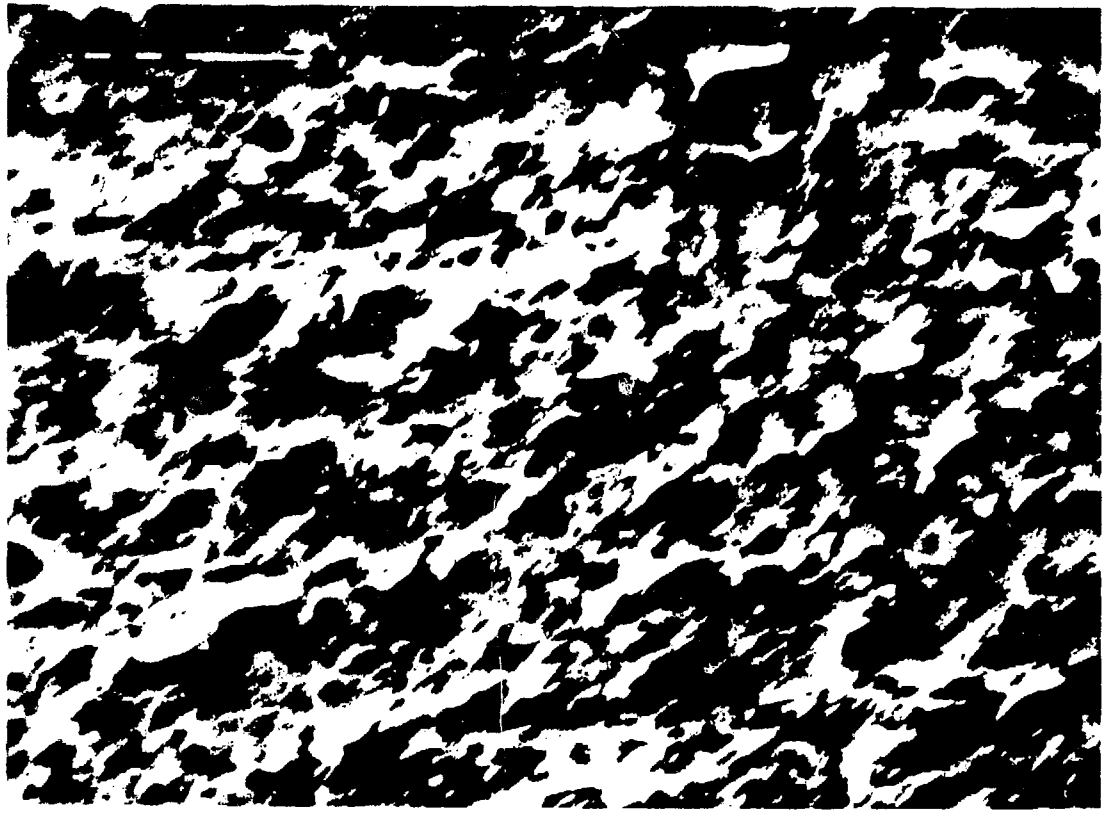

Fig. 4. The electron micrograph of a surface of the solid electrolyte Ag β-alumina.

and Crepy,[11] have used the scaling argument to find the following relation between the CPA exponent η and the fractal dimension:

$$\eta = 1/(d-1). \tag{3}$$

Since the scaling argument is not familiar to most investigators in electrochemistry, we will develop the theory based on a different model proposed by the present author.[14] The model, shown in Fig. 5, is constructed by connecting together the various stages of the Cantor bar in Fig. 3. Just like the Koch island model, the surface is assumed to be smooth in the direction perpendicular to the page, so the fractal dimension of this surface is $d = 1 + \ln 2/\ln a$. The model interface is self-affine, because self similarity is achieved when a part is magnified by an integral factor of a in directions parallel to the plane but by a factor of unity perpendicular to the plane.

The two sides of the interface can be assigned to metal and electrolyte in two ways, yielding two distinct physical models. In the first situation we assign the electrolyte to the black side to obtain a grooves within grooves model, which was inspired by De Levie's observation that polished metal surfaces exhibit grooves with jagged surfaces covered with smaller grooves.[7] When an ac signal flows from the electrolyte (black) into the electrode (white), it encounters ohmic resistance in the electrolyte and interfacial capacitance at the faces of every segment. The equivalent circuit of the interface is shown in Fig. 6. The circuit branches out at every new stage of the Cantor bar. The resistance increases by a factor of a at every branch because of the reduction in the width of the bar. The number of interfacial capacitors increases in proportion with the number of branches, but the size of the capacitors remains the same. This is an approximation which amounts to ignoring the interfacial capacitance in the dips between branches. One can see in Fig. 5 that at higher stages the areas in the dips become negligible compared with the areas of the sides. We have verified numerically that the capacitance of the dips does not affect the input impedance of the circuit at low frequencies. The common ground represents the electrode.

The input impedance of the network in Fig. 6 has the form of an infinite continued fraction:

$$Z(\omega) = R + \cfrac{1}{j\omega C + \cfrac{2}{aR + \cfrac{1}{j\omega C + \cfrac{2}{a^2 R + \ldots.}}}} \; . \tag{4}$$

The function $Z(\omega)$ satisfies the frequency scaling relation:[15]

$$Z(\frac{\omega}{a}) = R + \frac{aZ(\omega)}{j\omega C Z(\omega) + 2} \; . \tag{5}$$

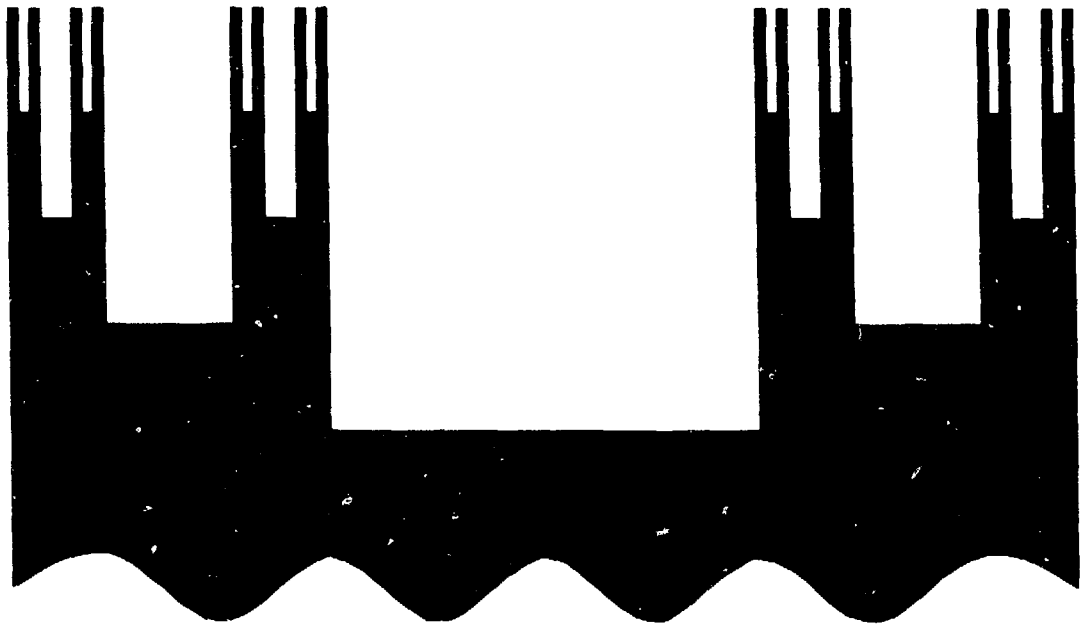

Fig. 5. A model of rough electrode-electrolyte interface based on the Cantor bar model.

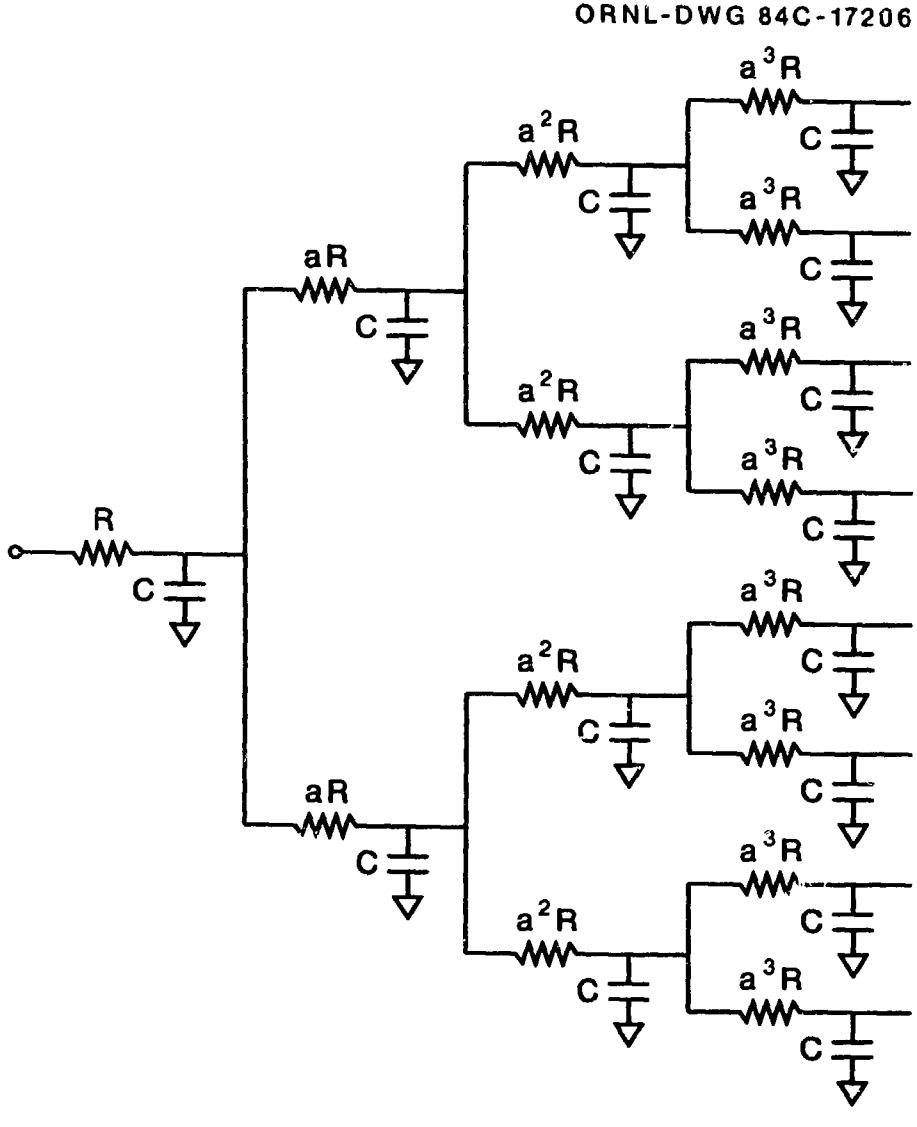

Fig. 6. The equivalent circuit of the model interface in Fig. 5.

In the low frequency limit Eq. 5 reduces to

$$Z(\frac{\omega}{a}) \simeq \frac{a}{2} Z(\omega) . \tag{6}$$

The relation in Eq. 6 is satisfied by

$$Z(\omega) = A(j\omega)^{-\eta} , \tag{7}$$

where A is a constant and

$$\eta = 1 - \ln 2/\ln a = 3 - d . \tag{8}$$

A smooth surface has $a \ll 1$ so that $\eta \to 1$ as observed.

The result in Eq. 8 is different from that in Eq. 3, and this generated some heated debate as to which one is the correct answer, because it was hoped that η was a universal function of the fractal dimension. We will show later that this is not the case because η depends on details of the surface geometry not measured by d. The insight leading to this conclusion as well as a physical understanding of the CPA behavior are gained from studying this primitive model.

As a start, we give a simple picture of the origin of the CPA behavior. We terminate the network after a finite number of stages and calculate the input impedance by using the recurrent relation method.[14] The results for the real part of $Z(\omega)$ are plotted in Fig. 7. At low frequencies the real part of Z reaches a plateau whose height increases by a factor of $a/2$ for every additional stage. At high frequencies the impedance has the limiting value R. Between these two limits the real part of the impedance exhibits the CPA behavior. The imaginary part of $Z(\omega)$ is inversely proportional to the frequency in both high and low frequency limits and has the power-law dependence in the middle range. These results show that the power-law frequency dependence is the result of competition between resistive and capacitive paths. We can look at Fig. 7 in a different way, namely that signals at lower frequencies tend to penetrate more stages of the network. This happens because a signal of lower frequency must propagate farther down the network before it finds sufficient capacitive paths to cross the interface. In doing so it also encounters higher resistance. In total it experiences a higher impedance than a signal of higher frequency. The self-similar structure ensures that the frequency dependence of the impedance follows the power-law. Real surfaces usually are self similar over a finite range of length scales, and this determines the frequency range in which the CPA behavior is evident.

The finite network calculation gives a concrete illustration of dynamical scaling. In Ref. 14 we showed that the impedance of a network with n stages has the following asymptotic expression at low frequencies $\omega RC \ll 1$ and large n:

$$Z_n(\omega) \simeq R \frac{a(a+1)}{(a-1)(a-2)(2a-1)} \left(\frac{a}{2}\right)^n + \frac{1}{2^n j\omega C} . \tag{9}$$

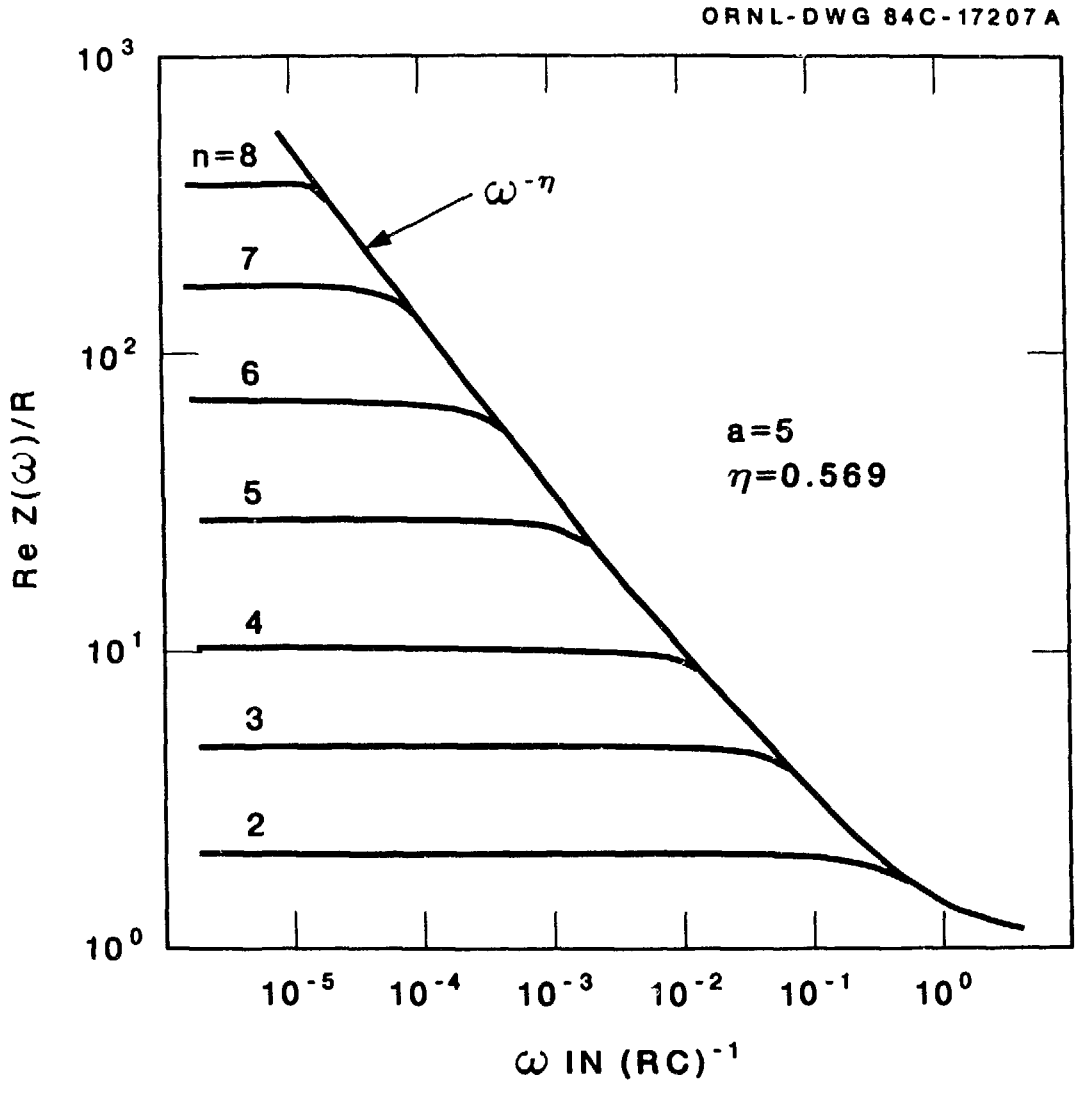

Fig. 7. The frequency dependence of the real part of the input impedance of the network in Fig. 5 after finite numbers of stages.

This equation means that for a signal frequency which penetrates n stages of the network, it experiences a resistance proportional to $(a/2)^n$ and a capacitance measured by 2^n. If we scale the frequency down by a factor of a, we deduce from Eq. 9 that, in the asymptotic regime,

$$Z_{n+1}(\frac{\omega}{a}) = \frac{a}{2} Z_n(\omega). \tag{10}$$

In the limit of large n there is negligible difference between Z_{n+1} and Z_n and the above equation reduces to the earlier result in Eq. 6. The relation in Eq. 10 can be interpreted in a different way, i.e. the signal with scaled down frequency can penetrate one more layer and thus experiences an impedance which is $a/2$ higher. Thus, the impedance is self similar, and is scaled up by a factor of $a/2$ when the frequency, which is used as the yardstick, is scaled down by a. The frequency exponent is the fractal dimension of the impedance.

We can now use the scaling argument to deduce the CPA exponent of the cylindrical surface generated by shifting the Koch island, assuming that the volume inside the cylinder is filled with electrolyte. For clarity we present the derivation put forward by Nyikos and Pajkossy.[16] We write, in analogy with Eq. 9 that for a surface with large but finite stages n

$$Z_n(\omega) \simeq R_n + 1/j\omega C_n \ , \tag{11}$$

for sufficiently small ω. The quantities R_n and C_n are difficult to calculate, but their scaling behavior can be found by simple arguments. If we increase the stage to $n+1$, the capacitance will scale according to the surface area, i.e. $C_{n+1} = \frac{4}{3} C_n$. The resistance is dominated by a newly added groove in the middle of each side. Since the width of the new groove is $1/3$ of the larger groove, the resistance is scaled up by $R_{n+1} = 3R_n$. This allows us to obtain

$$Z_{n+1}(\omega) = 3R_n + 3/4j\omega C_n = 3Z_n(4\omega) \ .$$

Or for $n \to \infty$

$$Z(\omega/4) = 3Z(\omega) \ . \tag{12}$$

This gives the relation between η and the fractal dimension d in Eq. 3.

The scaling argument points to the source of difference between the formulas in Eqs. 3 and 8, both of which link η to d. The frequency exponent depends on the scaling properties of two quantities, effective R and C. Both scale according to details in the geometric properties of the fractal and indepedently of each other. The fractal dimension is but one measure of the surface geometry. It is, therefore, not surprising that a unique relation between η and d is not possible. Keddam and Takenouti reached the same conclusion by studying an interface whose cross section is a Koch curve with generalized scaling ratios.[17]

We now discuss another exactly soluble model which demonstrates that η is not a universal function of d. The model is inspired by the electron micrograph

in Fig. 4 in which the irregularities are better described as bumps upon bumps. Shown in Fig. 8, the model is the product of two Cantor dusts, one associated with the x direction and one with the y direction.[18] We, therefore, named it the Cantor block model. As in the Cantor bar model, the figure shows the electrolyte protruding into the electrode. Every stage is a rectangular block, and in the most general case each block branches into $N_x N_y$ smaller blocks whose sides are scaled by $1/a_x$ and $1/a_y$ in the plane of the interface and $1/a_z$ in the perpendicular direction, $a_x > N_x$ and $a_y > N_y$. In the figure both N_x and N_y are equal to 2. The equivalent circuit of this model has the same structure as that in Fig. 2. The number of new branches at every stage is $N_x N_y$, and each branch consists of a series resistor and a capacitor connected to ground. The resistors scale up by $a_x a_y / a_z$ in each successive stage due to the reduction in cross-sectional area of the branch by $1/a_x a_y$ and the decrease in length by $1/a_z$. The capacitance is dominated by the contributions of the lateral surfaces, whose areas are reduced by factors $1/a_x a_z$ and $1/a_y a_z$ respectively in successive stages. Again, the input impedance can be expressed as an infinite continued fraction

$$Z(\omega) = R + \cfrac{1}{j\omega C + \cfrac{N_x N_y}{\frac{a_x a_y}{a_z} R + \cfrac{1}{j\omega \frac{C}{a_z}\left(\frac{1}{a_x} + \frac{1}{a_y}\right) + \cfrac{N_x N_y}{\left(\frac{a_x a_y}{a_z}\right)^2 R + \cfrac{1}{j\omega \frac{C}{a_z^2}\left(\frac{1}{a_x^2} + \frac{1}{a_y^2}\right) + \ldots}}}}} . \tag{13}$$

The impedance has the constant-phase behavior under a set of conditions, i.e. $a_x > a_y$, $a_x > a_z$, $a_x > a_z^2$, $a_y a_z < N_x N_y$, and $N_x N_y a_z < a_x a_y$. When all these conditions are fulfilled the frequency exponent is found to be

$$\eta = 1 - \ln(N_x N_y / a_y a_z) / \ln(a_x / a_z^2) \, . \tag{14}$$

The detail of this calculation is given in Ref. 18. The determination of the fractal dimension is subtle because the surface is self-affine and contains three scaling ratios a_x, a_y and a_z. According to Mandelbrot, the dominant scaling ratio is the one that gives the most rapid length reduction in the limit of large number of stages.[19] In the Cantor block model the dominant scale is a_x, so we measure the area using yard sticks of lengths 1, a_x^{-1}, a_x^{-2}, ..., a_x^{-n+1}, etc. At every stage we ignore features smaller than the yardstick. In this way the area at the nth stage is found to have the asymptotic value

$$A_n \propto (N_x N_y a_x^2 / a_y a_z)^{n-1} \, . \tag{15}$$

The fractal dimension is defined by $A_n \propto (a_x)^{(n-1)d}$, which yields

$$d = 2 + \ln(N_x N_y / a_y a_z) / \ln a_x \, . \tag{16}$$

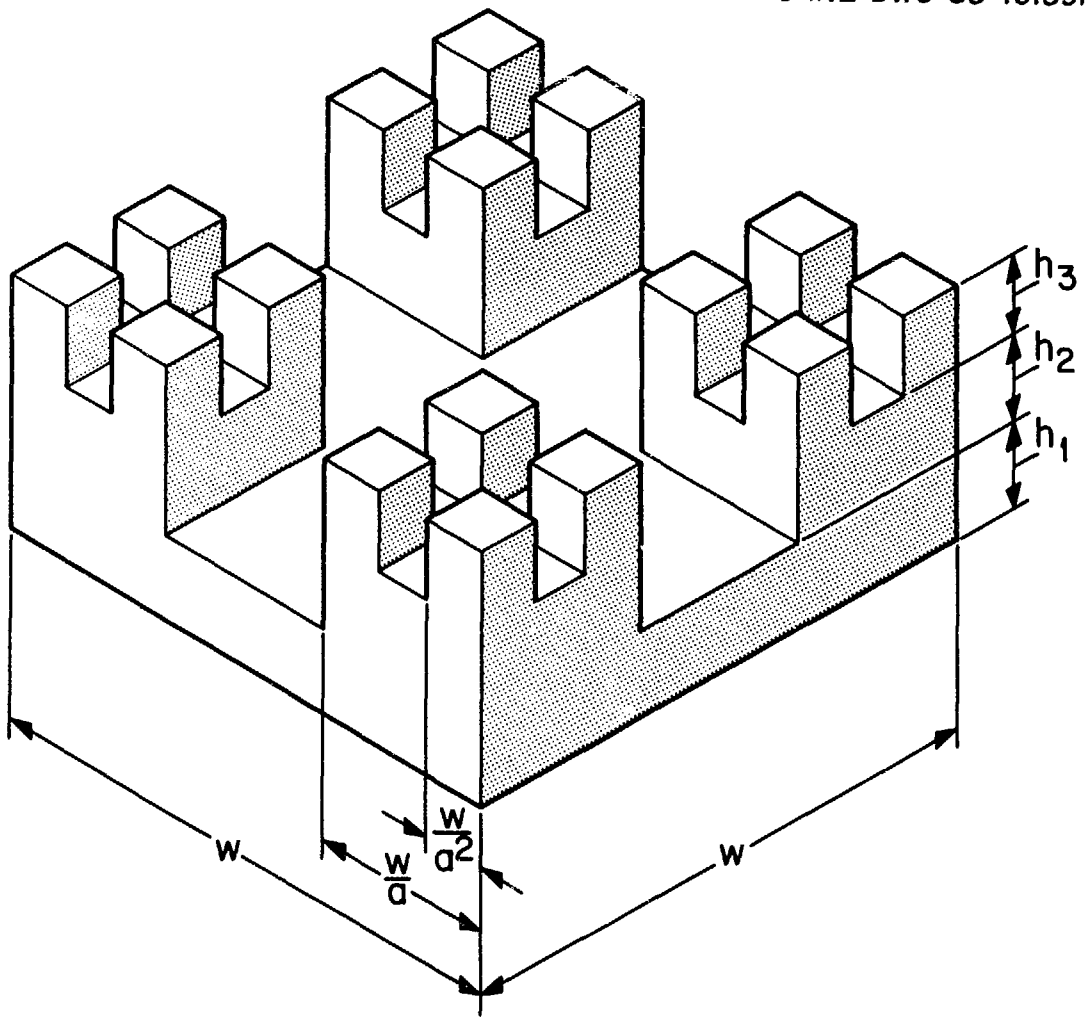

Fig. 8. The Cantor block model for rough electrode-electrolyte interface.

It is now quite apparent from Eqs. 14 and 16 that there is no univeral relation between η and d except the following inequality

$$\eta \leq 3 - d \,. \tag{17}$$

The Cantor dust models can be randomized, namely that the branching numbers and scaling ratios can be treated as random numbers with well-defined averages.[15] It has been found that randomization does not change the conclusions deduced for regular fractals, so it seems that the regular fractal models are more realistic than they may appear.

Bates and coworkers have put the various theoretical predictions to test by creating a set of rough electrodes and measuring their fractal dimensions and CPA exponents.[20,21] The electrodes were prepared from platinum and low resistance (0.007 Ω-cm) silicon with and without a thin gold coating. Pieces of platinum and silicon of $\simeq$ 1 cm^2 were polished using various grades of emery paper and alumina powder. When viewed at low magnification, the resulting surface finish had a definite lay, indicating that the roughness consisted of parallel grooves. The height profiles of the plates were measured using a profilometer equipped with an 0.5 μm diamond stylus. This instrument has a height resolution of 0.005 μm and a minimum horizontal step size of 0.04 μm. Several profiles were measured for each plate perpendicular to the lay at different positions near the center section, which was used in the electrical measurements. A typical profile is shown in Fig. 9. The profiles were analyzed by assuming that they are fractional Brownian curves, i.e. self-affine fractals whose scales in horizontal and vertical directions are related by $a_z = a_x^H$, where $H \leq 1$. To test of this hypothesis one calculates the structure function defined by

$$S(\delta) = \langle \Delta z^2(\delta) \rangle \,, \tag{18}$$

where $\Delta z(\delta) = z(x+\delta) - z(x)$ and $\langle\ \rangle$ denotes an average in the horizontal direction. If the profile is fractional Brownian, the structure function should be related to δ by[19]

$$S(\delta) \propto \delta^{2H} \,. \tag{19}$$

The data for two such profiles are shown in Fig. 10. It can be seen that the power-law relation in Eq. 19 is well satisfied for over one decade of δ in the submicron region, giving $H \simeq 0.9$ for both profiles. The range of length scale is limited by the resolution of the profilometer. The fractal dimension of the surface is related to H by $d = 3 - H$,[19] and this gives $d \simeq 2.1$. For reasons not yet fully understood, natural rough surfaces of all kinds, including the surfaces of the continents on Earth, have fractal dimensions around $d = 2.1$–2.2. After the profile measurements the plates were fixed onto glass substrates and wires were attached for impedance measurements.

The CPA exponents were determined by measuring the impedances with these electrodes immersed in 0.1 M H_2SO_4 solution. There is no theory for η for fractional Brownian surfaces, so we can only make qualitative comparison between experiment

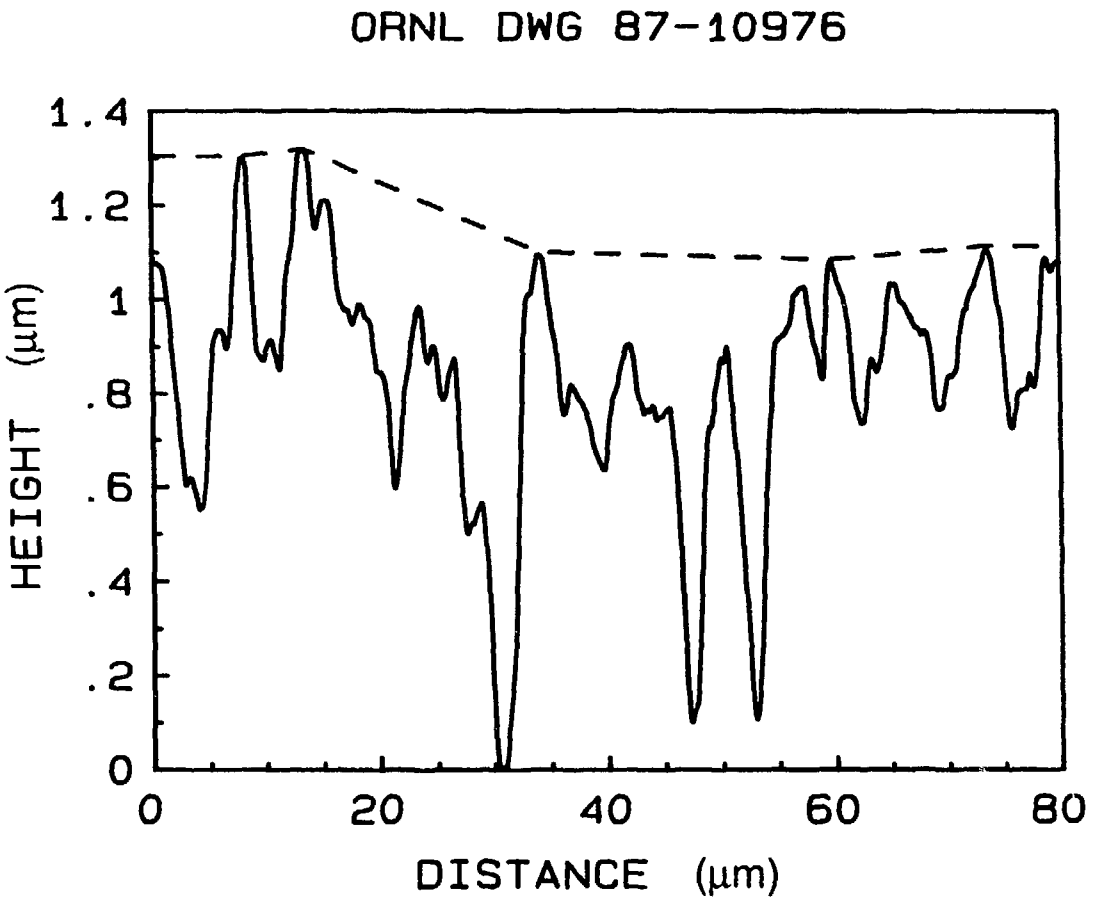

Fig. 9. Typical profile of a rough electrode created by polishing a solid surface with emery paper or alumina powder.

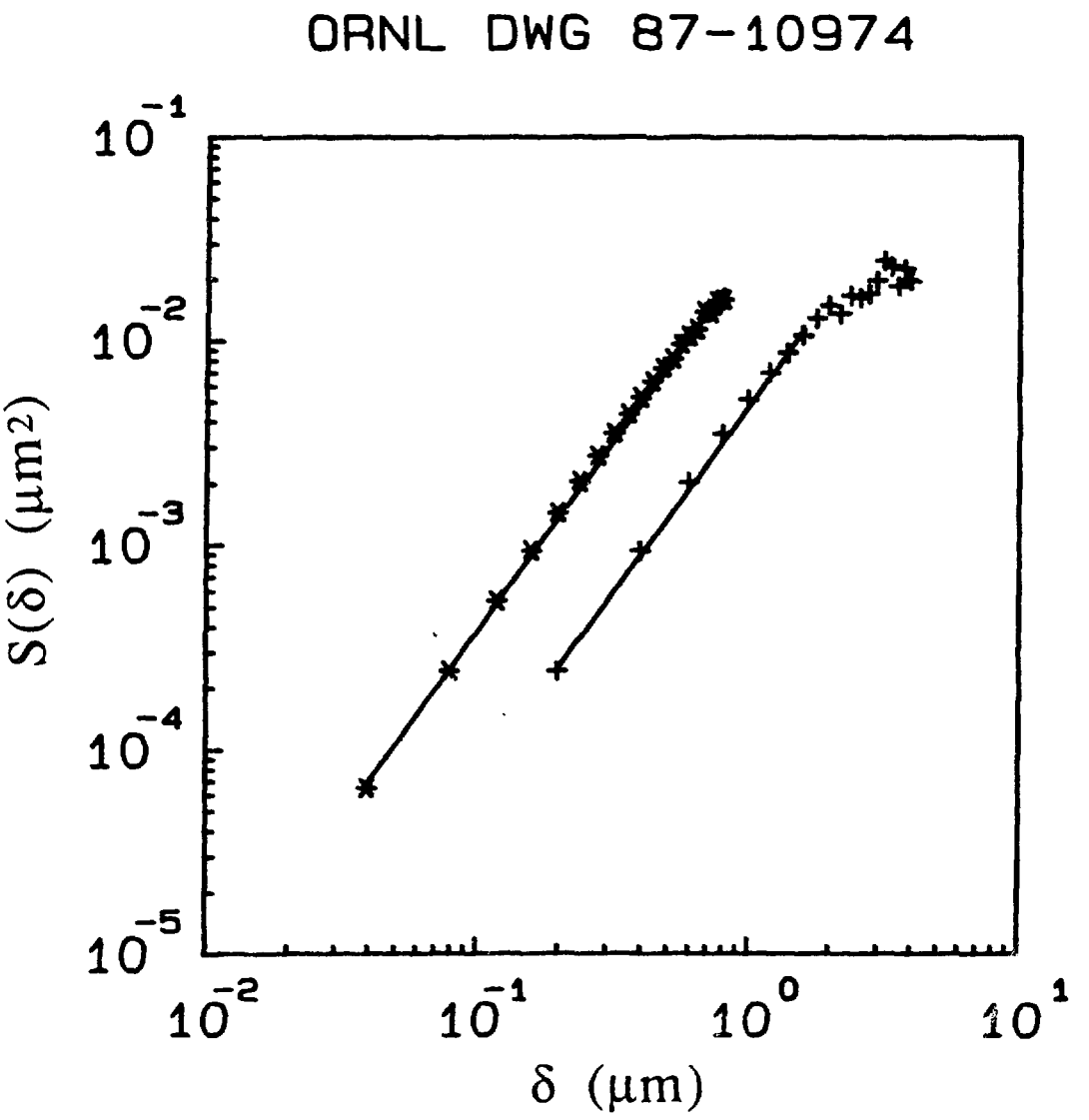

Fig. 10. The height-to-height correlation function of rough electrode profiles showing that they are well represented by fractional Brownian curves.

and theories. Since d is very close to 2, we can write $d = 2+\epsilon$, where $\epsilon = 1-H \ll 1$, both Eq. 3 and Eq. 8 give

$$\eta \simeq 1 - \epsilon = H \ . \tag{20}$$

We present the results of this study in an η versus H plot in Fig. 11. Each dot on the graph represents the result for one electrode, and the dashed line across the graph represents Eq. 20. The labels beside the points indicate how the electrode was prepared. For instance, Au/Si/600 was a gold-plated Si surface ground with 600 grit paper, and Pt/0.05 was a Pt surface polished with 0.05 μm alumina powder, etc. One can see clearly that there are points with almost equal H but very different η, and those with nearly equal η but very different H. Further examination reveals that Si and Pt surfaces form two distinct groups, i.e. the Si electrodes, whether coated with Au or not, have higher η than Pt electrodes. There is also a distinction in the shape of the protrusions in the surface, that hard Si surfaces tend to have more rounded protrusions than soft Pt surfaces. Therefore, the shape of the protrusion seems to play a strong role in determining the CPA exponent. Notice that the data are not inconsistent with Eq. 17, which can be written as $\eta \leq H$. On the other hand, Cantor dust type models are incapable of shedding light on the role of surface shape, because there is no clear way to relate the sharpness of the surface protrusions to any of the scaling parameters in the models. Further progress toward an analytical solution of the problem seems to be extremely difficult.

Bates and Chu reasoned that, under weak electric fields, the diffusion of ions in the electrolyte toward the electrode surface can be mapped onto the random walk problem, and the latter can be simulated by the Monte Carlo method. Assuming that a constant voltage is turned on across a CPE at $t = 0$, it follows that the current will have a time dependence given by $t^{-\eta}$ and the total charge given by

$$Q(t) \propto t^{1-\eta} \ . \tag{21}$$

The principle of the simulation is as follows. Random walkers are released from the counter electrode far away, and are allowed to migrate in the space between the electrodes. If a walker reaches the electrode, the migration time is recorded and another walker is released. A walker is discarded whenever it moves out of the space between the electrodes. By repeating this process a sufficient number of times, a set of data for $Q(t)$ is accumulated and the value of η can be extracted. The authors used the measured profiles for the electrode, but to save computer time, they argued that a line joining a few of the highest points of the profile, the dotted line in Fig. 9, is a good approximation for an equipotential surface so that random walkers can be released at random points on this line. While this approximation requires justification, the authors obtained values of η very close to the experimental values. The distinction between Si and Pt surfaces is clearly reflected in the results. There is one difficulty with the simulation procedure, however. As reported by the authors, they obtained $\eta \simeq 0.9$ for the cosine profile and 0.8 for the sawtooth profile. The sawtooth profile has been studied by Springer and Raistrick by numerically solving the Laplace equation for the potential and

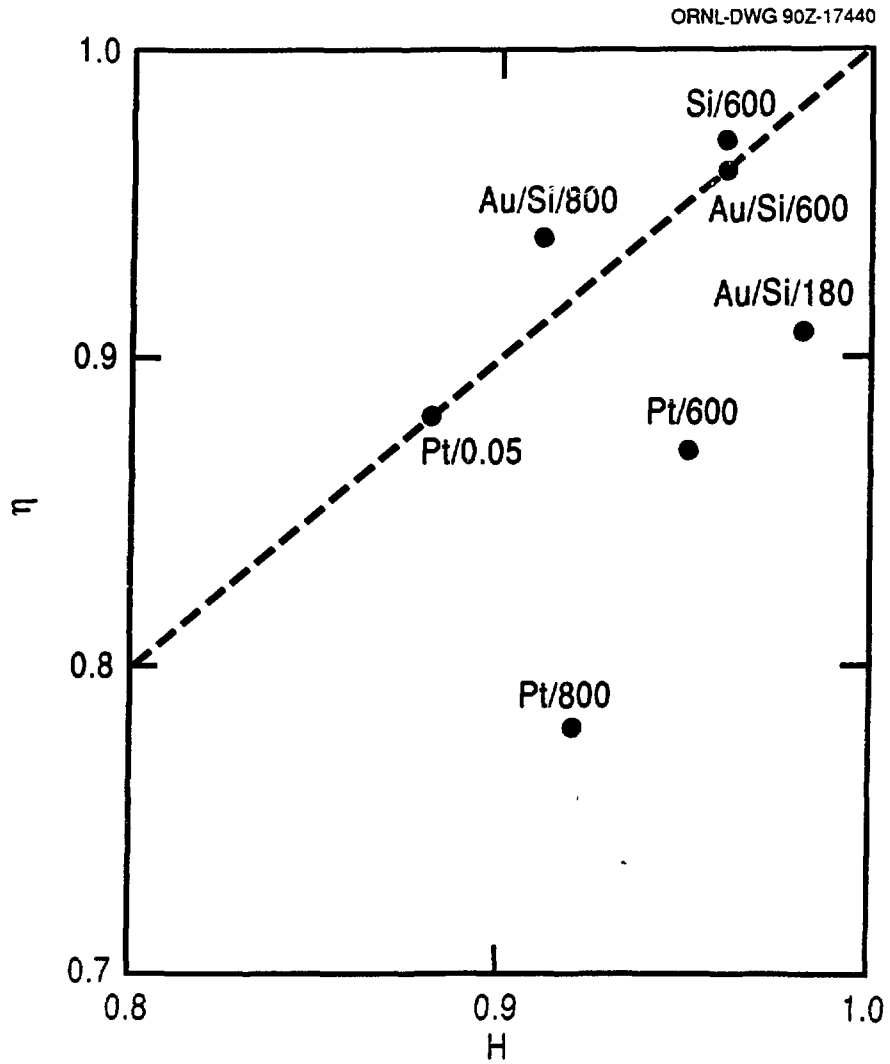

Fig. 11. The η versus H plot for several actual electrodes. The dotted line is the theoretical relation $\eta = H$.

current distributions.[22] The calculation gives $\eta = 1/2$ at low frequencies, indicating classical diffusion, and at high frequencies the real part of the impedance is constant and the imaginary part is inversely proportional to frequency. There is no nontrivial CPA behavior anywhere. It seems that the Monte Carlo simulation method should be used with caution, and more work is needed to verify the findings reported in Ref. 21.

3. Porous Electrodes

Porous electrodes are characterized by having open channels of all sizes extending into the bulk of the electrodes. One of the first models for such systems was constructed by reversing the sides of the electrode and electrolyte in the Cantor bar model in Fig. 5.[23] The black side is now the electrode, and the white side is a collection of channels which are filled with electrolyte. The electrical properties of each channel can be calculated by modeling it as a finite RC transmission line with a capacitance load at the end. The impedance of the entire system is found by combining the channels in parallel. Let the width of the widest channel be W, then in the next stage there are 2 channels of width W/a. In the third stage there are 2^2 channels of widths W/a^2, etc. It is convenient to consider a structure with $(M+1)$ stages and subsequently take the limit of infinite M. The length of the widest channel is Mh, where h is the height of each stage of the Cantor bar. Then the lengths of the next two stages are $(M-1)h$ and $(M-2)h$ respectively. Consider a channel of length $L_m = mh$. The input admittance of the channel is[24]

$$Y_m = \frac{\alpha_m}{r_m}\frac{r_m + \alpha_m Z_L(m)\tanh(\alpha_m L_m)}{r_m \tanh(\alpha_m L_m) + \alpha_m Z_L(m)}, \tag{22}$$

where $\alpha_m = (j\omega r_m c_m)^{1/2}$, r_m and c_m are the resistance and capacitance per unit length respectively, $Z_L(m)$ is the impedance of the end capacitance. For the widest channel, $m = M$, we set $r_M = r$ and $c_M = c$. Then the scaling relation between the channels gives $r_m = a^{M-m}r$, $c_m = c$, $\alpha_m = \alpha a^{(M-m)/2}$, $\alpha = (j\omega rc)^{1/2}$, $Z_L(m) = a^{M-m}Z_L$, and $Z_L = 1/j\omega C'$, with C' being the interfacial capacitance of the flat end of the widest channel. The input admittance of the entire structure is

$$Y_{M+1}(\omega) = \sum_{m=1}^{M} 2\Big(\frac{2}{a^{1/2}}\Big)^{(M-m)}\frac{\alpha}{r}\Big(\frac{ra^{-(M-m)/2} + \alpha Z_L \tanh(\alpha hma^{(M-m)/2})}{ra^{-(M-m)/2}\tanh(\alpha hma^{(M-m)/2}) + \alpha Z_L}\Big). \tag{23}$$

The quantity of interest is the low-frequency behavior of the total admittance in the limit of $M \to \infty$. A few simplifying approximations are now apparent. In the limit of large M and m the load impedance is unimportant because the line is much longer than the wavelength. Furthermore, the lengths of the mth stage and the $(m+1)$th stage are approximately equal. This allows us to deduce the following frequency scaling relation

$$Y(\frac{\omega}{a}) = \frac{2}{a}Y(\omega), \tag{24}$$

where $Y(\omega)$ is the limit of Eq. 23 when $M \to \infty$. The above equation is satisfied by $Y(\omega) \propto (j\omega)^{\eta}$, where

$$\eta = 1 + \ln 2 / \ln a = 3 - d \,, \tag{25}$$

and d is the fractal dimension of the interface. The series in Eq. 23 converges in the limit of infinite M provided that $2 < a^{1/2}$. Recall that $Y(\omega)$ is the inverse of the impedance $Z(\omega)$, we have shown that the inverse Cantor bar is a CPE.

The inverse Cantor bar suggests another model, which consists of long channels bounded by simple curves such that there are $1, N, N^2, \ldots$ channels with cross sections scaled by $1, a^{-2}, a^{-4}, \ldots$. One can show that as long as $a < N < a^{3/2}$, the set of transmission lines is a CPE with $\eta = 2 - \ln N / \ln a$.[23] The area of the pores is a fractal with dimension $d = 1 + \ln N / \ln a$. Thus the relation $\eta = 3 - d$ is obeyed. Randomizing the pore numbers and pore sizes does not affect the relation between η and d.

The physical origin of the CPE in the multi-channel models is substantially the same as in the branching models. High frequency signals tend to follow the wide, low impedance channels while low frequency signals are forced to seek out the more numerous, narrow, and high impedance channels. The shift of the effective current paths with frequency plus the geometric scaling of the paths lead to the power-law frequency dependence of the total impedance.

The geometry of porous solids is not limited to long and non-crossing channels. Sapoval and his coworkers have made an exhaustive study of many soluble geometries.[25] They obtained the same result for the multi-channel models as discusssed above. Their results for several sphere upon sphere models are particularly interesting. Just like the Cantor dust models, these can also be mapped onto series-parallel branching networks, and analyses of their input impedance again demonstrate that η is not simply related to d. There are fractal surfaces with no CPA behavior and CPE surfaces which are not fractal. Geometrical details are important, but it is not yet clear to what extent one can apply these understandings to naturally occuring porous materials.

In principle, there is another frequency regime of interest, at sufficiently low frequencies where the diffusion length in the electrolyte is comparable to the size of the electrode. The electric response is controled by the diffusion process, and even ideal flat electrodes have the CPA exponent $\eta = 1/2$. It was shown by Pajkossy and Nyikos[26] and by Sapoval *et al.*[25] that for a fractal electrode of dimension d the following simple relation exists:

$$\eta = (d - 1)/2 \,. \tag{26}$$

In the Faradaic regime where electrochemical reaction takes place, one expects different values of η for the same fractal interface. This problem has been discussed by Le Méhauté[27] and by Sapoval *et al.*[25]

4. Theory of Bulk CPE

To appreciate the mystery of the bulk CPA behavior in ionic conductors, we first discuss the classical theory of the ac response of such a material. Ionic conductors are a special kind of ionic solids in which one species of ions, usually the cation, can migrate within the lattice. At sufficiently high temperatures vacancies are created by thermal activation. Electrical conduction becomes possible when an electric field drives mobile ions into vacancies nearby. In doing so they leave new vacancies behind and other ions can move into them. One can equally well describe the conduction process as vacancy diffusion. Because the paths of vacancy migration tend to zigzag through the crystal, there is an ohmic resistance associated with this process. Also, the collection of ions of opposite charges can be polarized by an electric field, creating a capacitive element. The resistive and capacitive elements, R and C, are in parallel, so that the input impedance has the expression

$$Z(\omega) = \frac{R}{1 + j\omega RC} \,. \tag{27}$$

By separating the real and imaginary parts, one finds that the real part is frequency independent for $\omega \ll (RC)^{-1}$ and falls off like ω^{-2} for $\omega \gg (RC)^{-1}$, while the imaginary part behaves like ω and ω^{-1} respectively in these two limits. Therefore, the CPA behavior as observed experimentally is outside the scope of the classical theory. Attempts have been made to model the CPA behavior by invoking a continuous distribution of activation energies,[1,4] but this type of effort does nothing to advance our understanding of the origin of the CPE.

The bulk CPA behavior is but one manifestation of the universal $1/f$ fluctuation seen in many systems, such as sun spot activities, traffic flow, the flow of sand in an hour glass, and the flow of electric current through a resistor.[28] In recent years we have seen accelerated progress toward better understanding of the $1/f$ fluctuation, and there is widely held believe that the phenomenon is akin to what is taking place at the critical temperature of second order phase transition, i.e. that systems that undergo $1/f$ fluctuations have no natural length scale, and thus are self-similar under scale transformations. We will show that this so-called 'self-organized criticality' concept may also be a good starting point for elucidating the bulk CPA problem.[29–31]

Let us consider a simple, one-dimension model for ionic conductor, shown in Fig. 12. The larger ions define the lattice while the smaller ions are mobile. The classical picture for ionic conduction through vacancy migration is depicted in Fig. 12(a). In Fig. 12(b) we consider a new mode of conduction, that when driven by an electric field, it is possible to find two ions in the same interstitial space temporarily. These two repel each other so strongly that they both move out of that interstitial position and cause two nearby interstitials to be doubly occupied, as shown in Fig. 12(c). Thus, the relaxation of one doubly occupied site creates two doubly occupied sites. In the next step, the relaxation of the two doubly occupied sites results in three doubly occupied sites, etc. As the process continues more doubly occupied sites are

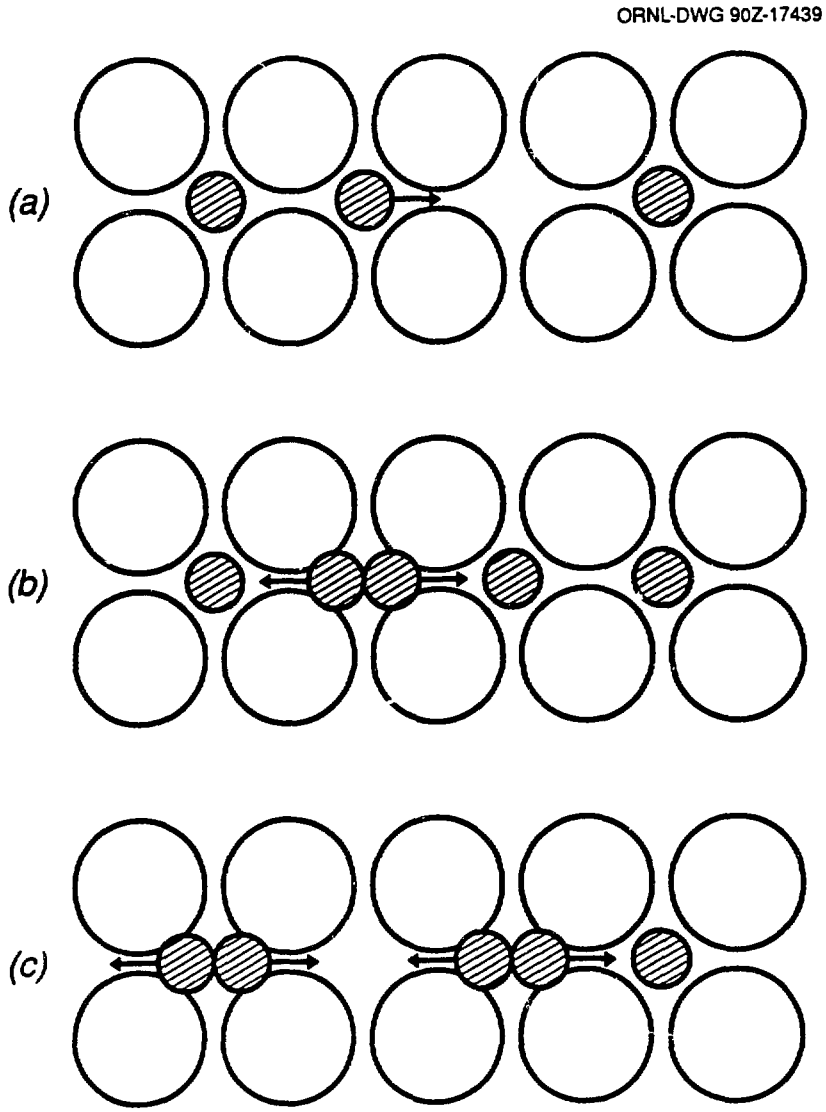

Fig. 12. Simple model for ionic conduction in fast ion conductors. (a) A schematic representation of vacancy diffusion. (b) A doubly occupied lattice position in which the two ions experience strong mutual repulsion. (c) Both ions move out of the initial position into neighboring positions on opposite sides, causing two positions to be doubly occupied.

created at every new step until a boundary site is reached, at which point one ion is ejected out of the solid. Afterwards, the system heals itself by slowly returning to singly occupied sites. This mode of conduction is governed by a set of dynamical rules. Let q_i be the charge at the mobile ion site labelled by i, then the site is stable if $q_i \leq 1$ and unstable otherwise. For an unstable site the charge redistributes according to

$$q_i \rightarrow q_i - 2,$$
$$q_{i\pm1} \rightarrow q_{i\pm1} + 1 \, . \tag{28}$$

If there are more than one unstable site at any moment, they are relaxed simultaneously. The charge is allowed to flow out at the boundary so that the entire system will eventually return to a stable state. In this way the new conduction mechanism maps exactly onto the sand pile problem first studied by Bak *et al.*[29-31]

In higher dimensions there are more than two nearest neighbors in any lattice of interstitial positions. Two ions in the same interstitial site can move in many possible ways into two neighboring positions. This problem has not yet been studied. Our present knowledge of higher dimensional systems comes from a slight variation of the model as follows. Consider a regular lattice in a D-dimensional space whose lattice points are $\mathbf{R}_l$. The lattice points represent the sublattice of the mobile ions, and $q(\mathbf{R}_l)$ is the charge at the site $\mathbf{R}_l$, which has m nearest neighbors. The site is stable if $q(\mathbf{R}_l) \leq m$ and unstable otherwise. For an unstable site the dynamical rules of charge redistribution are

$$q(\mathbf{R}_l) \rightarrow q(\mathbf{R}_l) - m,$$
$$q(\mathbf{R}_l + \delta_i) \rightarrow q(\mathbf{R}_l + \delta_i) + 1 \, . \tag{29}$$

In the above equation δ_i for $i = 1, 2, ..., m$ denote the set of vectors linking a lattice point to its nearest neighbors. In the event that many sites are unstable, they all relax simultaneously. The charge is allowed to flow out of the boundary.

To simulate a conduction process one should inject extra charges at one end of the system and collect charges flowing out of the other end. The time sequence of charge flow, when properly Fourier analyzed, would give information on the frequency response of the system. This has not yet been done. What has been done is a simulation of the diffusion problem in which every lattice point has a higher than stable amount of charge.[32] The square lattice ($m = 4$) enclosed in a square boundary has been studied in detail. In Fig. 13 we show the final charge distribution starting from the unstable situation where $q = 5$ at every site. Only one quadrant of the square is shown, where the center of the square is at the lower left corner. The values of q at various points are coded as follows: 1 by squares, 2 by diamonds, 3 by open circles, and 4 by open space. There is a complex pattern of nonuniform charge distribution which consists of a set of nesting heart shapes along the diagonal. This pattern is created during the process when excess charges flow out of the boundary. The ratios of the linear measures of the nearest pair of heart shapes are rational approximations of the irrational quantity $(3 - \sqrt{5})/2$, which is

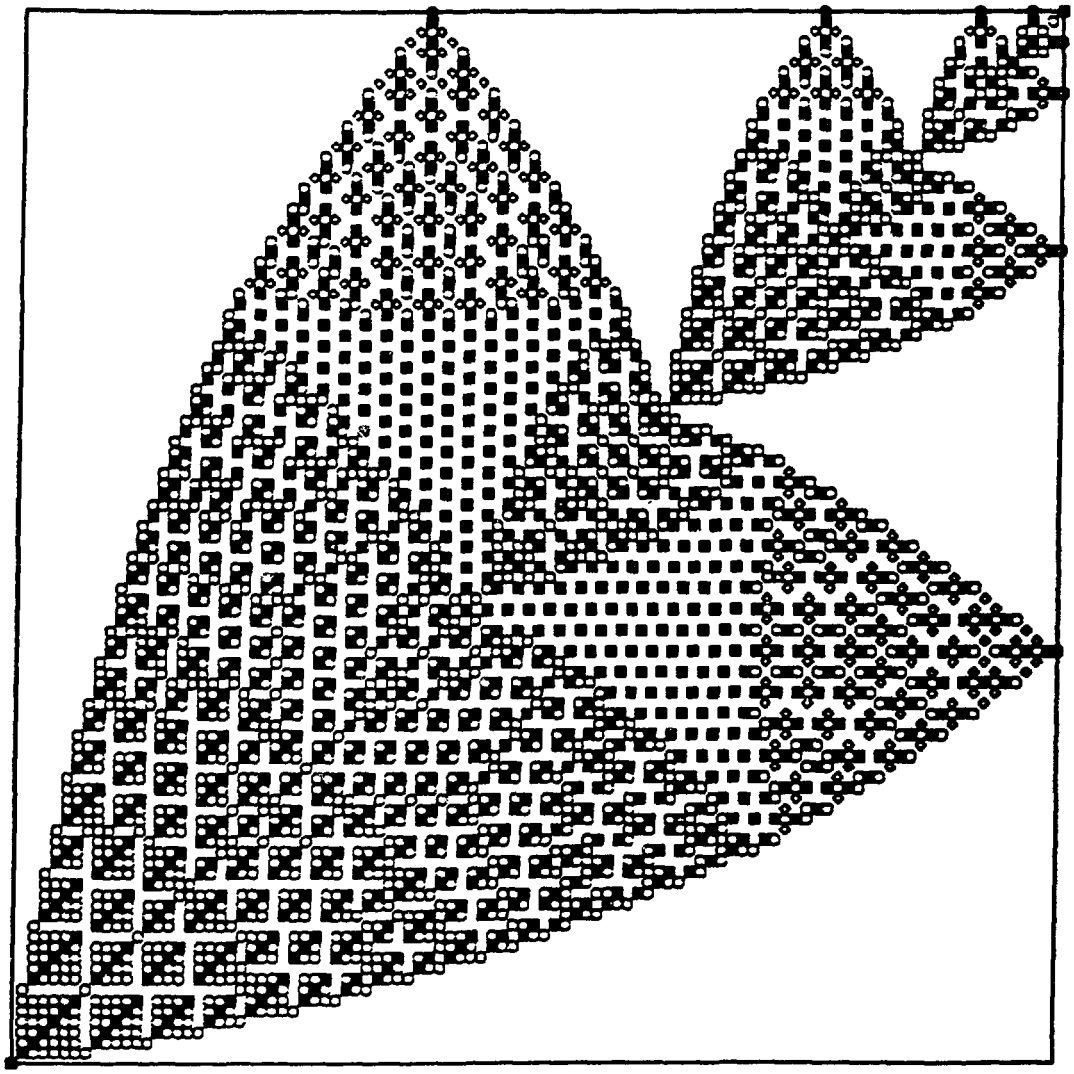

Fig. 13. Final charge distribution of a square lattice with initial charge $q = 5$ at every point. Only one quadrant is shown, with the center of the square at the lower left corner. The values of q are coded as follows: 1 by squares, 2 by diamonds, 3 by open circles, and 4 open space.

the classic Golden Section ratio. What is relevant to the conduction problem is the time sequence of the total outward flow, which is plotted in Fig. 14 for a 801×801 square system. The time is measured by the number of iteration steps. At the beginning the total flow follows the $t^{1/2}$ law, indicating that the flow obeys the law of classical diffusion. Later in the process the flow slows down and the total charge takes on a different power-law time dependence with the exponent 0.40, as shown in the insert of Fig. 14. This behavior is known as anomalous diffusion, and we will show that this behavior is linked to CPA behavior in the conduction process.

In classical diffusion the total charge $Q(t)$ is proportional to $t^{1/2}$. When such a system is driven by a constant external voltage, the current follows the Ohm's law and the total charge $Q(t) \propto \epsilon$. In the anomalous situation the diffusive process obeys the law $Q(t) \propto t^{\nu}$. By using the scaling argument, we infer that when driven by a constant voltage the charge will be given by $Q(t) \propto t^{2\nu}$. It follows from Eq. 21 that the CPA exponent is given by

$$\eta = 1 - 2\nu \, . \tag{30}$$

For the square system under discussion, we find $\nu = 0.4$ so that $\eta = 0.2$. We have also carried out the simulation for the cubic lattice bounded by cubic boundaries and obtained $\nu = 0.25 \pm 0.01$ and $\eta = 0.50 \pm 0.02$. It is not clear at present whether this number depends on the lattice structure. Perhaps all one can conclude from this study is that the new conduction mechanism may lead to a CPE with $\eta \simeq 0.5$. This number is small compared with $\eta = 0.77$ for amorphous Li_3PO_4. Crystalline conductors tends to give smaller values of η, typically around 0.6.[1]

Examination of the intermediate patterns during the charge relaxation process reveals an intimate connection between anomalous diffusion and the growth of the complex pattern in the final state. In Figs. 15–18 we show four intermediate patterns for the square system with starting charge $q = 5$ at every site. Very early in the relaxation process the uniform distribution quickly breaks down into plane waves with crests of $q = 6$ and troughs of $q = 4$ as shown in Fig. 15. A rudimentary heart shape develops at the corner, and it interacts with the waves and changes the crest and trough values to 5 and 3. A thin strip of $q = 4$ separates the front of the waves from the boundary. As time progresses the wave front moves toward the boundary, and upon reaching it ejects a pulse of charge. Afterwards the wave front retreats toward the center until it reaches the tip of the heart shape. At this point the motion reverses itself and the shape grows by one grid point. At a later time, shown in Fig. 16, the shape has grown in size, and smaller shapes have formed following the wake of the leading one. The growth of the nonuniform region causes the width of the wave front to shrink and the distance traversed by the wave front to lengthen. Consequently, every time the wave front returns to the boundary, it ejects a pulse that is two units less than the previous one, and the interval between successive pulses increases by two units. The total flow after t iterations is given by

$$Q(t) = \sum_n [N - 2(n-1)]\delta_{t,n^2-n+1} \simeq Nt^{1/2} \tag{31}$$

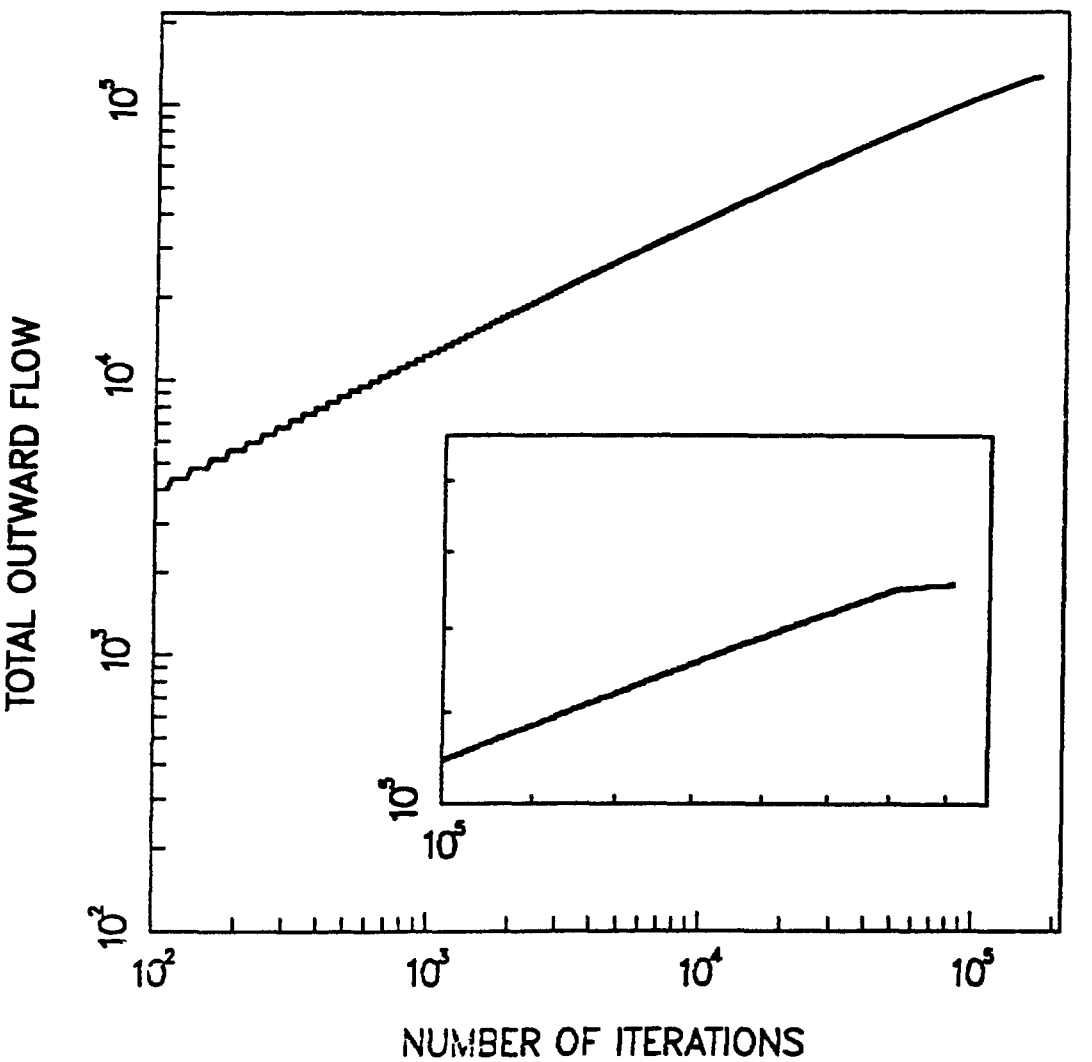

Fig. 14. The charge distribution after 160 iterations of the square grid with initial charge $q = 5$ at every point. In addition to the four codes used in Fig. 13, we present 5 by pluses, 6 by crosses, and 7 and 8 by asterisks. It requires 10,738 iterations to reach the final pattern in Fig. 13.

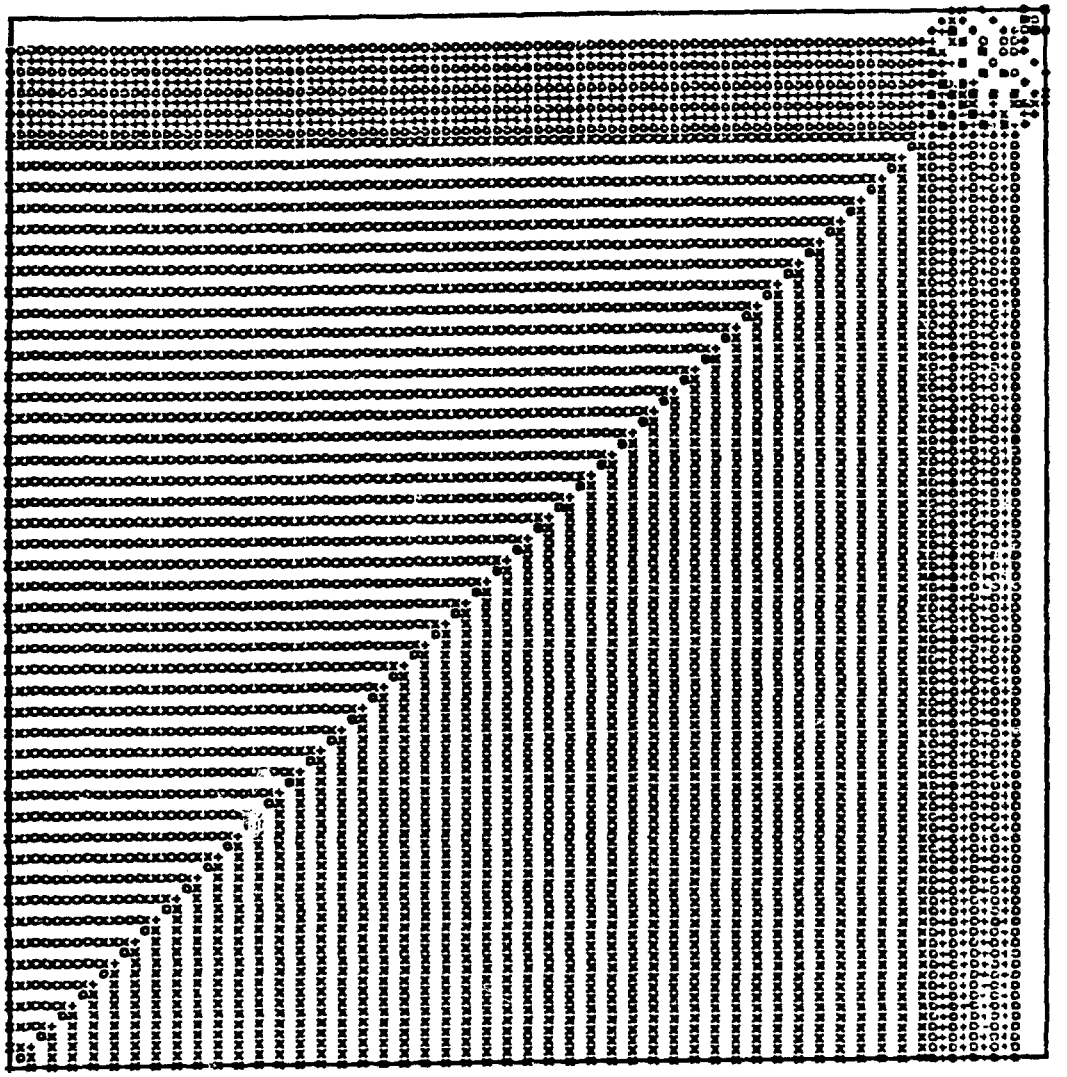

Fig. 15. Same as Fig. 14 but after 1320 iteration steps.

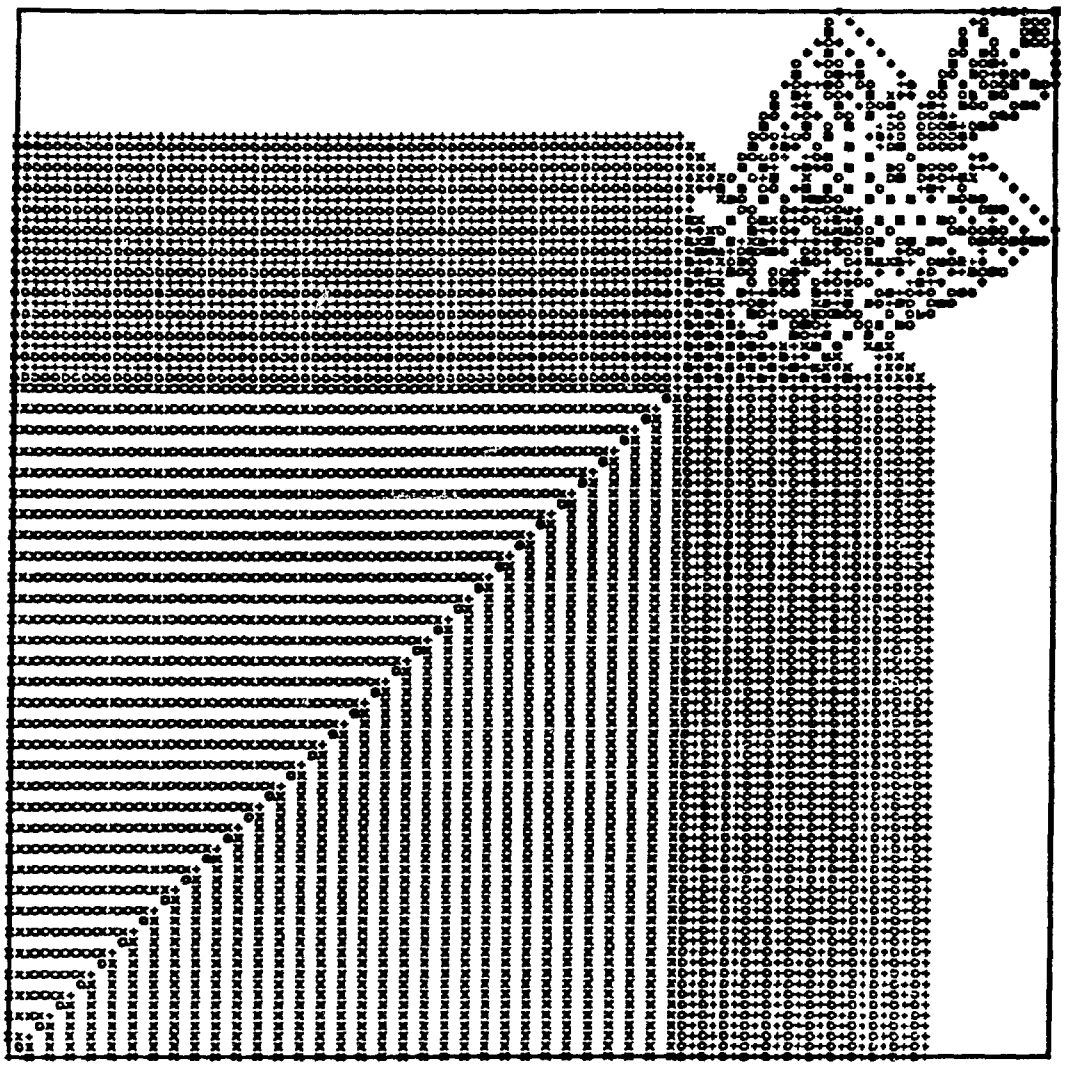

Fig. 16. Same as Fig. 14 but after 2608 iteration steps. Waves of anomalous diffusion begins to show clearly.

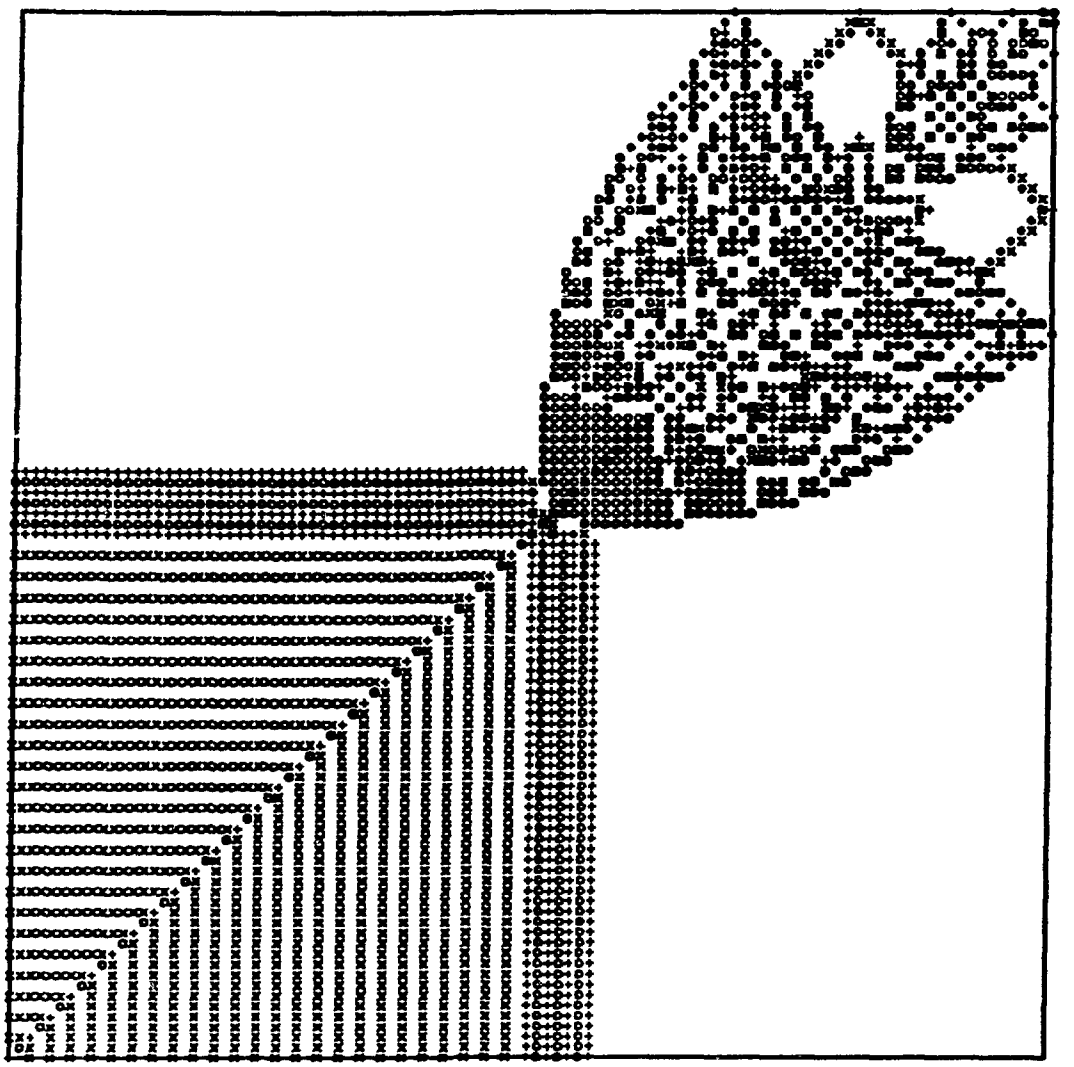

Fig. 17. Same as Fig. 14 but after 9690 iteration steps. Anomalous component of charge diffusion now dominates the flow.

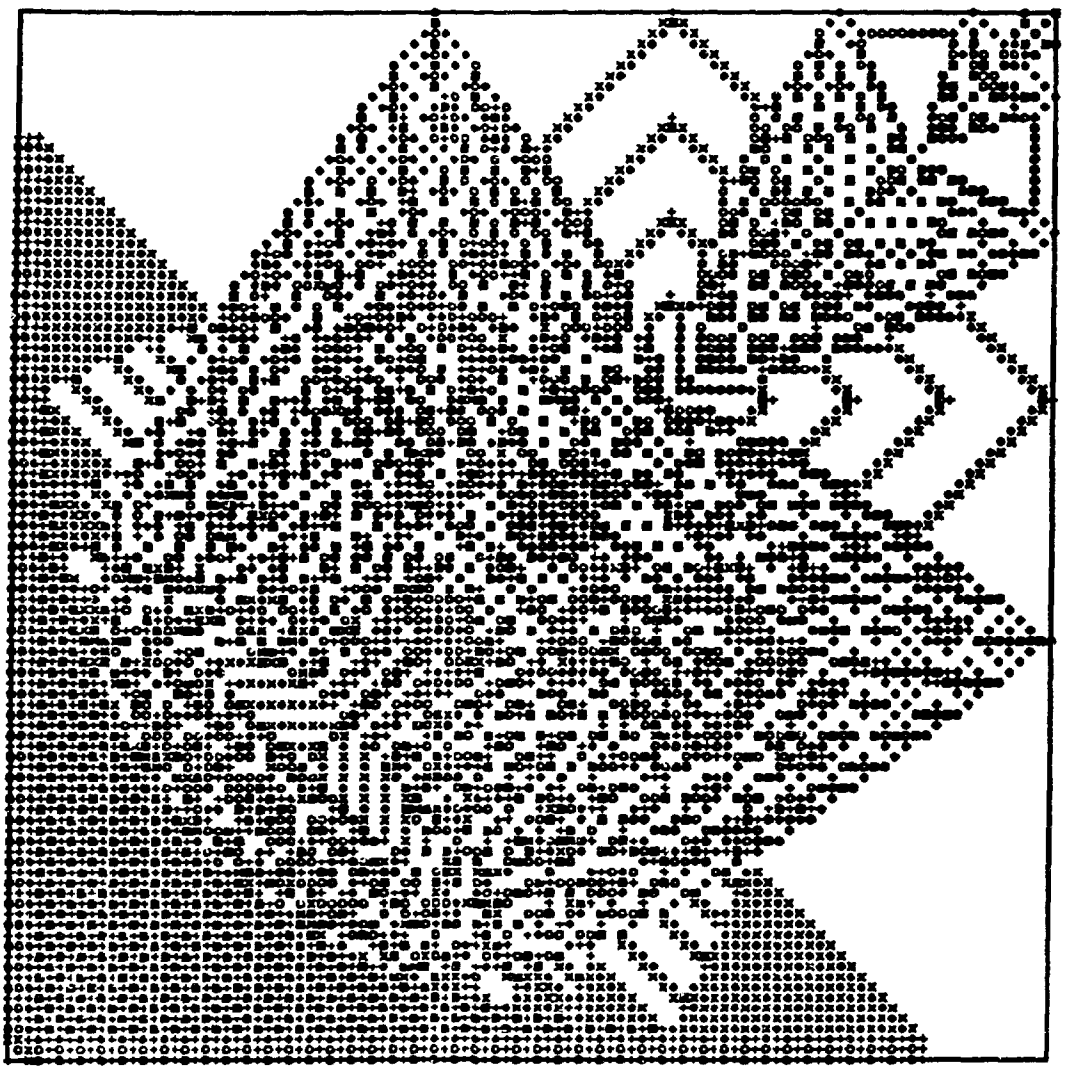

Fig. 18. Total outflow of charge $Q(t)$ for a 801×801 square lattice as a function of t = iteration steps. The insert shows the flow during the last half of the relaxation process, showing the $t^{0.4}$ law of anomalous diffusion.

for $1 \ll t \ll N$. In the above equation N is the size of the boundary, n sums over the sequence of pulses, and the Kronecker δ indicates that the nth pulse emerges at $t = n^2 - n + 1$. This contribution can be identified as the classical component of the diffusion process.

As the nonuniform region grows to about one-half of its final size, shown in Fig. 17, we can clearly see waves flowing toward the boundary in the region between some of the shapes. The wave fronts make 45° angles with the boundary. The excess charge in these waves must first flow through the leading shape, and are ejected at the boundary sporadically. We identify this as the emerging anomalous diffusion component. Near the end, shown in Fig. 18, the classical diffusion component becomes insignificant and the anomalous component dominates the total flow. This sequence of events demonstrates that the anomalous behavior is due to charge flow through the nonuniform part of the intermediate distribution. The flow is self-similar in time because the nonuniform region is self-similar in space. We conclude that the anomalous diffusion behavior comes from charge flow through a self-generated self-similar distribution of vacancies.

Much more work needs to be done to clarify many important issues, chief among which is a direct simulation of conduction process based on a more realistic model whose margin of stability is $q = 2$. We believe that this line of inquiry will yield a deeper understanding of the origin of bulk CPE.

5. Acknowledgments

The author wishes to thank J. B. Bates for suggesting the series of investigation of interface and bulk CPE, to Theodore Kaplan for a critical reading of the manuscript, and to A. A. Kornyshev for his invitation to discuss our work at the Working Party on Electrochemistry held at the International Centre of Theoretical Physics in Trieste, Italy in 1990. This review grew out of the notes of that lecture. The research was supported by the U.S. Department of Energy, Division of Basic Energy Research, under Contract No. DE-AC05-84OR21400 with Martin Marietta Energy Systems, Inc.

References

1. J. B. Bates, *unpublished data.*
2. Bates, J. C. Wang, and Y. T. Chu, *J. Non-Crystalline Solids* (to appear); and references cited therein.
3. J. C. Wang and J. B. Bates, *Solid State Ionics* **18&19**, 224 (1986).
4. J. C. Wang and J. B. Bates, (to be published).
5. I. Wolfe, Phys. Rev. **27**, 755 (1926).
6. P. H. Bottelberghs, in *Solid State Electrolytes* (Academic Press, New York, 1978) pp. 145–172.

7. R. de Levie, *Electrochimica Acta* **10**, 113 (1965).
8. P. H. Bottelberghs and G. H. J. Broers, *J. Electroanal. Chem.* **67**, 155 (1976).
9. R. D. Armstrong and R. A. Burnham, *J. Electroanal. Chem.* **72**, 257 (1976).
10. J. B. Bates, J. C. Wang and Y. T. Chu, *Solid States Ionics* **18&19**, 1045 (1986).
11. A. Le Méhauté and G. Crepy, *Solid State Ionics* **9&10**, 17 (1983).
12. B. B. Mandelbrot, *Fractals: Forms, Chance and Dimension* (Freeman, San Francisco, 1977).
13. B. B. Mandelbrot, *The Fractal Geometry of Nature* (Freeman, San Francisco, 1983).
14. S. H. Liu, *Phys. Rev. Lett.* **55**, 529 (1985).
15. T. Kaplan and L. J. Gray, *Phys. Rev.* **B32**, 7360 (1985).
16. L. Nyikos and T. Pajkossy, *Electrochimica Acta* **30**, 1533 (1985).
17. M. Keddam and H. Takenouti, *Electrochimica Acta* **33**, 445 (1988).
18. T. Kaplan, L. J. Gray and S. H. Liu, *Phys. Rev.* **B35**, 5379 (1987).
19. B. B. Mandelbrot, in *Proceedings Sixth International Symposium on Fractals in Physics* (North Holland, Amsterdam, 1987).
20. J. B. Bates, Y. T. Chu and W. T. Stribling, *Phys. Rev. Lett.* **60**, 627 (1988).
21. J. B. Bates and Y. T. Chu, *Solid State Ionics* **28–30**, 1388 (1988).
22. T. E. Springer and I. D. Raistrick, *Calculation of Electrochemical Impedances by Solution of the Laplace Equation using Green's Boundary Integral Method*, abstract presented at the First International Symposium on Electrochemical Impedance Spectroscopy, Bombannes, France, 22–26 May, 1989.
23. T. Kaplan, S. H. Liu and L. J. Gray, *Phys. Rev.* **B34**, 4870 (1986).
24. R. B. Adler, L. J. Chu and R. M. Fano, *Electromagnetic Energy Transmission and Radiation* (Wiley, New York, 1965).
25. B. Sapoval and J.-N. Chazalviel and J. Peyriére, *Phys. Rev.* **A38**, 5867 (1988).
26. T. Pajkossy and L. Nyikos, *Electrochimica Acta* **34**, 171 (1989).
27. A. Le Méhauté, in *The Fractal Approach to Heterogeneous Chemistry* (Wiley, New York, 1989), pp. 311–328.
28. For a review of $1/f$ noise, see W. H. Press, *Commun. Mod. Phys.* **C7**, 103 (1978).
29. P. Bak, C. Tang and K. Wiesenfeld, *Phys. Rev. Lett.* **59**, 381 (1987).
30. C. Tang and P. Bak, *Phys. Rev. Lett.* **60**, 2347 (1988).
31. P. Bak, C. Tang and K. Wiesenfeld, *Phys. Rev.* **A38**, 364 (1988).
32. S. H. Liu, T. Kaplan and L. J. Gray, *Phys. Rev.* **A42**, 3207 (1990).